J Mater Sci (2010) 45:1695–1708
DOI 10.1007/s10853-009-4160-x

Evolution of microstructure and mechanical properties during quenching and tempering of ultrahigh strength 0.3C Si–Mn–Cr–Mo low alloy steel

Fawad Tariq · Nausheen Naz ·
Rasheed Ahmed Baloch · Ashraf Ali

Received: 19 November 2009 / Accepted: 21 December 2009 / Published online: 5 January 2010

Abstract Effects of quenching and tempering treatments on the development of microstructure and mechanical properties of ultrahigh strength 0.3C Si–Mn–Cr–Mo low alloy steel were investigated. Samples were austenitized at 1123–1323 K for 2400 s and oil quenched (OQ) to produce mixed microstructures. Tempering was carried out at 473–773 K for 2–3 h. Phase transformation temperatures were measured using dilatometer. The microstructures were characterized using optical and scanning electron microscope. SEM–EDS analysis was carried out to determine the type and size of non-metallic inclusions. Volume percent of retained austenite was measured by X-ray diffraction technique. Hardness, tensile properties, and impact energies were also determined for all heat treated conditions. Fractography of impact specimens were done using stereomicroscope and SEM. The results showed that newly developed steel exhibited peak hardness, yield strength, and tensile strength of about 600 HV, 1760 MPa, and 1900 MPa, respectively, when OQ from 1203 K and tempered in between 473 and 573 K, combined with adequate ductility and impact toughness. Decrease in hardness and strength was observed with increasing tempering temperature whereas the impact energy was stable up to 623 K, however, impact energy was found to decrease above 632 K due to temper martensite embrittlement.

Introduction

Quenched and tempered (Q&T) low alloy steels are the most widely used, studied, and discussed steels due to their inherent high strength and toughness combination (because of hard phase martensite) obtained by relatively simple hardening and strengthening heat treatment, and their suitability and adaptability in many structural applications particularly in automobile, aerospace, and space industry. Depending on the alloy content of the steels and the section size of the part being quenched, various microstructures will be obtained in the as-quenched condition. Higher alloy contents and decreasing section sizes (increasing cooling rates) promote the formation of martensite whereas the moderate to slower cooling rates favors the formation of bainite, pearlite, and ferrite, which form at higher temperatures. All the parameters involved in a particular heat treatment process like the austenitization temperature and time, the quench medium and cooling rate, and the tempering temperature, and time affects the final microstructure of the steel. The microstructure in turn controls all the properties that a particular alloy exhibits.

Ultrahigh strength Q&T low alloy steels (like AISI 4141, AISI 4330, AISI 4340, 300 M, D6AC, AFNOR 15CDV6, etc.) have been in existence for many years and are being used in aircraft undercarriages, airframe parts, pressure vessels, missile applications, gun barrels, gears, bolts, springs, screws, machinery parts, connecting rods, crank shafts, etc. [1–9] because of their high strength and toughness along with ease of fabrication, welding, and simple heat treatment procedures. With the increase in demand for ultrahigh strength applications of low alloy steel, there exists a continual search and exploration of possible alloy properties which fulfills the requirements successfully and more economically. The idea behind this work was to develop

---

F. Tariq (✉) · N. Naz · R. A. Baloch
Materials Research and Testing Laboratory, Pakistan Space and Upper Atmosphere Research Commission (SUPARCO), 75270 Karachi, Pakistan
e-mail: t_fawad@hotmail.com

A. Ali
Material Engineering Department, NED University of Engineering and Technology Karachi, 75270 Karachi, Pakistan

steel which is comparable to existing ultrahigh strength low alloy steels in terms of composition and properties.

In this connection, relatively new medium carbon low alloy steel with a nominal composition of 0.3%C–1.5% Si–1.1%Cr–0.8%Mn–0.45%Mo–0.2%Ni was developed. When used in Q&T condition, this alloy exhibits high strength combines with good ductility and toughness at room temperature. Although a lot of work has been done by many researchers on various aspects of ultrahigh strength low alloy steels but to the best of the author's knowledge, no study was found in the literature focusing directly on the evolution of microstructure and mechanical properties during Q&T treatment of 0.3%C Si–Mn–Cr–Mo steel. The objective of this work was, therefore to study in detail the effects of variation of Q&T treatments on the resulting microstructure and mechanical properties of this steel. Emphasize was placed on low to medium temperature tempering (i.e. 473–773 K) treatments to retain much of the hardness and strength rather than toughness. Another objective of this investigation was to develop a Q&T cycle for this steel that results in ultrahigh strength combined with sufficient toughness and plastic deformation behavior required for ultrahigh strength applications.

Material and experimental procedure

Experimental material

The investigation was conducted on 0.3%C Si–Mn–Cr–Mo low alloy steel produced by electric arc melting furnace, chemically fine tuned in ladle furnace and vacuum degassed to reduce the volatile gas contents. Molten steel was then continuous cast into billet and then subsequently hot rolled into bars of 100 mm diameter after several passes. The chemical composition of the steel bar used in this study was determined through spark emission spectrometer as shown in Table 1.

Dilatometry

Austenite start (As or Ac_1), Ac_3, and austenite finish (Af) temperatures were measured using standard dilatometric technique. Cylindrical longitudinally oriented samples of 6 mm diameter and 25 mm length were machined from the annealed sheet. A high temperature Orton dilatometer (model 1600D) was used with a resistive furnace supported by quartz rods enclosed in a test chamber. The samples were heated to 1523 K at a rate of 283 K/s. The temperature of the sample was measured with thermocouple spot welded to its outer surface. The length change of the sample during heating was monitored by a LVDT. There was no quenching facility available with the dilatometer, therefore only heating curve was present in this work. Martensite start (Ms) temperature was calculated to be approximately 623 K by the empirical relationships postulated by Steven and Haynes [10] and Krauss [11].

Heat treatment procedures

The as-rolled steel bar was then annealed at 1073 K for 1 h in electric resistance-type heating furnace. The heating rate was kept at 373 K/h and temperature variation was within ±5 K. Square samples of about 20 × 20 × 10 mm were cut from the bar for Q&T treatments and metallographic examination. Samples were austenitized above Ac_3 temperature at different temperatures ranging from 1133 to 1323 K for 40 min and oil quenched (OQ) to produce mix microstructure. 1203 K and 1273 K were selected as austenitizing (hardening) temperatures for further tempering treatments. Higher austenitizing temperature ensured fullest possible transfer of the alloying elements and retained carbide into the solid solution. Tempering was carried out in range of 473–773 K for 2 and 3 h followed by air cooling. All heat treatments were carried out under protective atmosphere of nitrogen gas to avoid surface decarburization.

Microscopy

Microstructure of as-received steel bar was examined for non-metallic inclusions (NMI) in as-polished condition. Samples where cut along the rolling direction and surface parallel to the rolling direction was ground and polished using standard metallographic techniques. Sizes and shapes of the NMIs were measured by image analyzing software as per ASTM E 45-97 and type of the inclusions were detected through SEM–EDS analysis. Microstructural examinations of all heat treated conditions were carried out using optical microscope and JEOL JSM6380A SEM equipped with EDS. Metallographic samples were prepared by adopting standard mounting, mechanical grinding, and polishing techniques. Observations were made after etching with a 2% nital solution. ASTM grain sizes were determined as per ASTM E 112-96 with the aid of image analyzing software.

Table 1 Average chemical composition (in wt%) of low alloy steel used in this work

Elements	C	Si	Mn	Cr	Mo	Ni	V	S	P	Cu	Fe
Composition (wt%)	0.32	1.5	0.85	1.13	0.43	0.23	0.10	≤0.01	0.02	0.13	Bal.

Martensite packet size was measured as the effective grain size for Q&T samples [12–14].

The heat-tinting technique was used to distinguish retained austenite (γ), bainite (α_b), and martensite (α_M) phases in the as-quenched samples. Unmounted polished samples were lightly etched with 2% nital and heated in electric resistance heating furnace in air at 473 K for 2 h and then cooled to room temperature. With this technique, the various phases appear as different colors (contrast change) under the microscope. This method enabled us to measure the vol% of the different phases using image analyzer.

X-ray diffraction

Quantitative measurements of the vol% of retained γ and α_M present in microstructure were carried out on suitably prepared samples using a Siemens D5000 X-ray diffractometer. All the X-ray measurements were carried out in step scan mode with step size of 0.02, time per step of 3 s and angular interval 35°–90°. CuK$_\alpha$ (1.54056 Å) radiation filtered with Ni was used with 40 kV and 20 mA with monochromator. The integrated intensities of the $(111)\gamma$, $(110)\alpha$, $(200)\gamma$, $(200)\alpha$, $(211)\gamma$, and $(211)\alpha$ peaks were used in the direct comparison method to determine the vol% of retained γ and α_M [15]. The accuracy of determinations was about ±1%. The average C content of the retained γ was estimated from the lattice parameter measured from the $(111)\gamma$, $(200)\gamma$, and $(211)\gamma$ XRD peaks. The lattice parameter was converted to C content using the relationship suggested in [16].

Mechanical testing

Vickers macrohardness measurements, made with a 100 kg load for 30 s on a suitably prepared surface, were used to monitor hardness changes during all Q&T treatments. In addition to macrohardness, microhardness measurements were also carried out on all heat treated and prepared samples. Microhardness measurements were carried out at 500 g load, 12 s dwell time and ×500 magnification. All macro and microhardness data reported in this paper represent the average of at least five measurements per sample.

Tension tests were conducted on standard sub-size specimens of rectangular cross section having 50 mm gage length, 6.3 mm width and 5 mm in thickness as per ASTM E 8-99, cut from the longitudinal direction. All the tension tests were performed on 150 kN universal tensile testing machine at a load rate of 0.50 kN/s at room temperature. Average of at least two tensile tests for each testing condition was reported here.

Impact tests were carried out on charpy V-notch (L–T orientation) standard sub-size specimens (5 × 10 × 55 mm) as per ASTM E 23-98 on pendulum-type impact testing machine using 300 J hammer. At least two charpy impact specimens were fractured at room temperature for all heat treated conditions. Fractography was conducted on fracture surfaces cut off the impact-tested samples under stereomicroscope and JEOL JSM6380A SEM to determine the type and mode of fracture. Elemental mapping of intergranularly fractured facets was carried out in back-scattered (BSE) mode using SEM–EDX to elucidate the effect of grain boundary impurities on embrittlement.

Results and discussion

Dilatometry

From the results of dilatometry shown in Fig. 1, it was observed that the normal thermal expansion of the sample took place during heating of the sample from room temperature to 1053 K. Austenite start (As) or Ac$_1$ temperature peak was observed at about 1053 K, Ac$_3$ temperature peak was observed at 1123 K and the austenite finish (Af) temperature peak was observed at about 1463 K. The Ac$_1$–Ac$_3$ segment implies the occurrence of $\alpha \rightarrow \gamma$ transformation which led to length contraction as a result of γ formation. Si was responsible for higher austenitic transformation temperatures of this steel [17].

Non-metallic inclusions

Figure 2 showed the optical and SE micrographs of as-polished surface, revealing the morphologies and types of NMIs. It was seen from Fig. 2a–c that the inclusions were isolated and globular in shape and their sizes vary in range from 10 to 50 µm. Inclusions were found randomly distributed, however, inclusion nests were also observed at some regions (Fig. 2f). Both Type A (sulfide) and Type C (oxide-silicate) inclusions were recognized as per ASTM E-45. Generally, every inclusion has it own characteristic

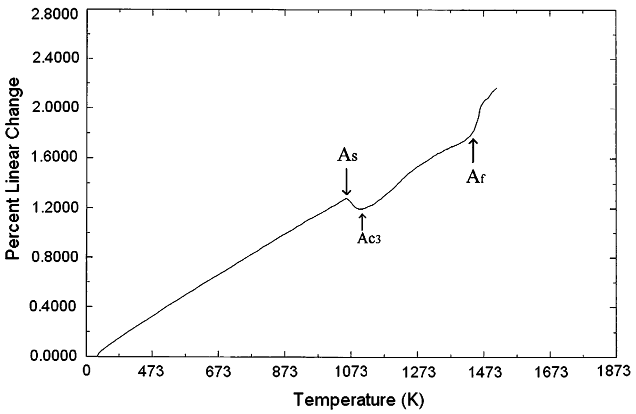

Fig. 1 Dilatometric curve of steel sample showing phase transformations occurring during continuous heating

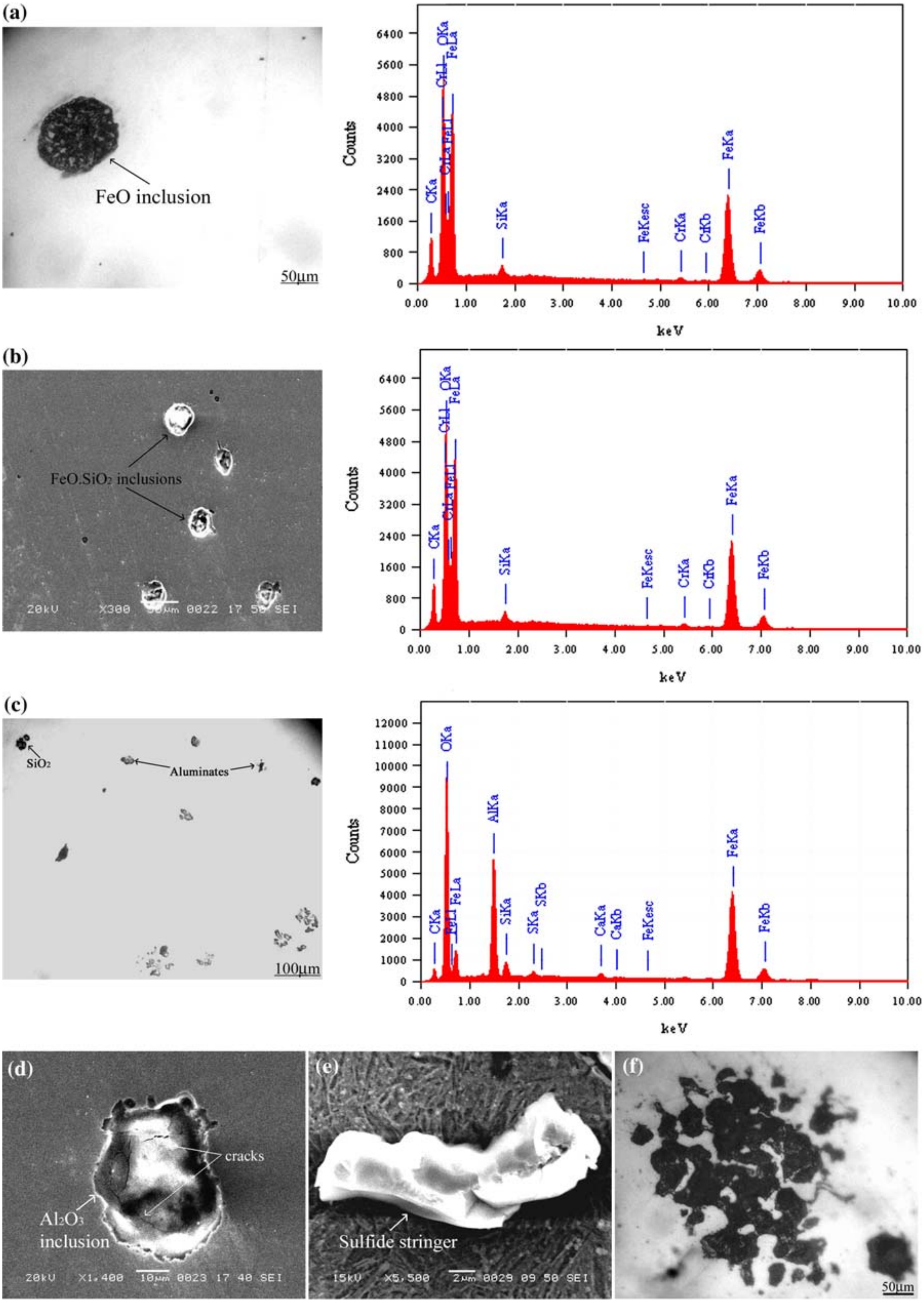

Fig. 2 Optical and SEM pictures of NMIs with their EDS results. **a** Globular FeO inclusion, **b** globular, isolated FeO-SiO_2 inclusions, **c** Al_2O_3 and SiO_2 inclusions, **d** brittle Al_2O_3 inclusion with internal cracks, **e** deformed sulfide stringer, and **f** inclusions nest

shape and appearance which can be seen at different magnifications [18, 19]. Oxide and silicates inclusions are non-deformable (Fig. 2c) whereas sulfide inclusions (FeS, MnS, etc.) are deformable. EDX results showed that the NMIs in the steel were mostly oxides of Fe, Al, and Si, with round morphology or obtuse angle. Mostly globular iron oxide inclusions were found (Fig. 2a), whereas the SiO_2 inclusions (dark black with glassy appearance) were occasionally found at some places (Fig. 2c). Al_2O_3 inclusions were found spherical in shape and brittle, as seen in Fig. 2d. These were deoxidation products and were introduced during steel making practice (i.e. indigenous). Al_2O_3 and $SiO_2{\cdot}Al_2O_3$ type of NMIs were believed to enter into molten metal from slag or during deoxidation with Al or Si. Al_2O_3 inclusions could also enter in steel during tapping of molten metal from ladle/tandish into continuous caster. Sulfide inclusions usually precipitated during solidification process due to high S content in the melt. Beside inclusions, sulfide stringers (discontinuous and light gray in color) were also observed elongated in the direction of rolling (Fig. 2e). Stringer (Type S) of up to 38 μm in length and 23 μm in width were observed. Because inclusions of various sizes, shapes, and types were present and randomly distributed, it was therefore very difficult to measure the inclusion number accurately, however, an attempt was made and the inclusion number was measured to be 1.5–2.0.

The presence of variety of inclusions and high inclusion number indicated the inadequate cleanliness of the alloy; even though the steel was vacuum degassed before continuous casting. These inclusions adversely affect the fracture toughness and fatigue strength of the steel [20]. They act as stress raisers and are potential sites for crack nucleations and microvoids. Weak bonding between the inclusion/matrix interface results in the formation and opening of void. Also, cracks in brittle inclusion or in matrix adjacent to the inclusion are created as a result of plastic deformation [18, 21, 22]. Therefore, for applications requiring high toughness, "ultraclean" steel should be produced through electro-slag remelting technique (ESR).

Microstructures

Optical micrographs of OQ samples from various austenitizing temperatures were shown in Fig. 3. ASTM grain size number was measured to be 9.5 (12–15 μm grain dia.) for 1133 K and 1203 K OQ samples. It was seen in Fig. 3a that the 1133 K OQ sample consists of mixture of acicular ferrite (α_{ac}) and lath martensite (α_M). Polygonal ferrite (nucleated from grain boundaries) and retained γ was also observed in this structure. Presence of large amount of randomly distributed α_{ac} was attributed to the high inclusion content of this steel. Acicular ferrite usually nucleates heterogeneously from inclusions and grows into plate-shaped morphology (as seen in Fig. 3a). Figure 4a showed the vol% of α_{ac} with respect to austenitizing temperatures. The microhardness measurements were also made for each OQ condition and

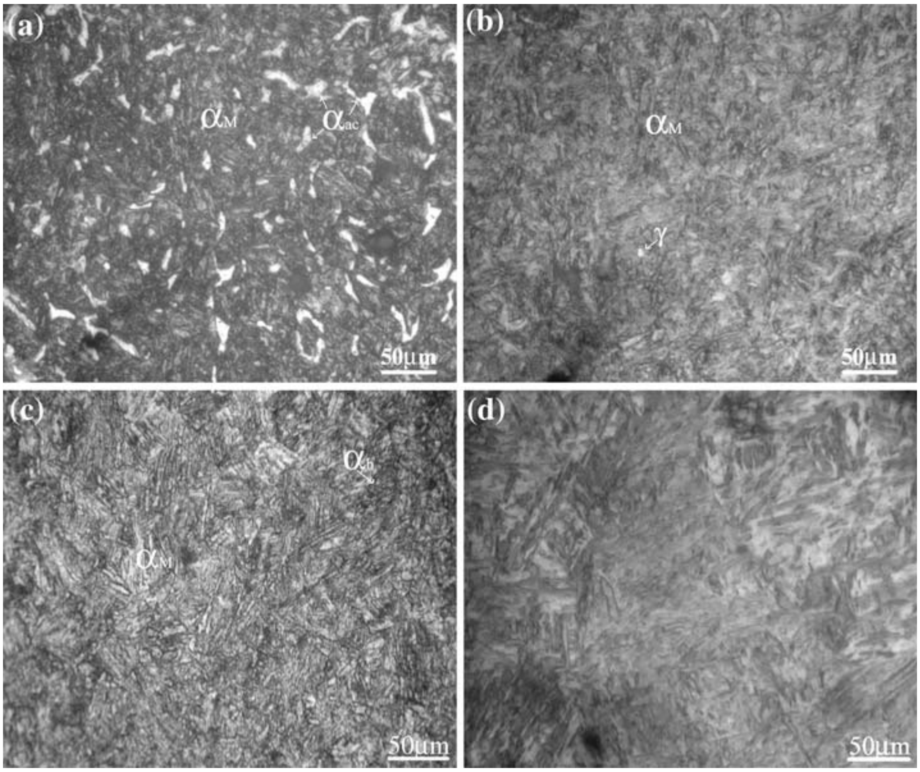

Fig. 3 Optical micrographs of OQ samples, austenitized at various temperatures for 2400 s. **a** 1133 K, **b** 1203 K, **c** 1273 K, and **d** 1323 K (α_M martensite, α_{ac} acicular ferrite, α_b bainitic ferrite, γ retained austenite)

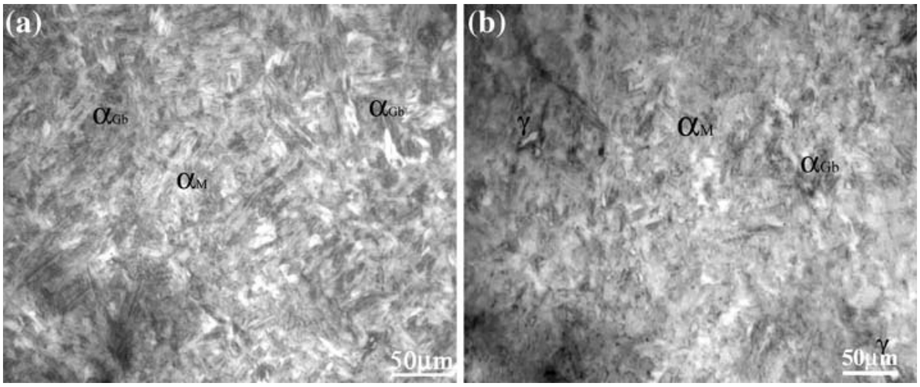

Fig. 4 Graph showing influence of austenitizing temperature on **a** vol % of α_{ac} and **b** microhardness of OQ samples

average values were shown in Fig. 4b. Microhardness was found increasing with increasing austenitizing temperature up to 1203 K and then decreased (Fig. 4b). Initial rise in hardness was attributed to the decrease in soft α_{ac} phase with subsequent increase in hard α_M phase with increasing temperature. However, after an optimum austenitizing temperature (i.e. 1203 K), decline in hardness was observed with further rise in temperature because of γ grain growth, as shown in Fig. 3d. Microstructure of the 1203 K OQ sample consists of α_M with high dislocation density (Fig. 3b). Block-type γ was also observed in Fig. 3b which was retained during quenching because of medium C, Mn, and high Si content of the steel. Acicular or polygonal α was not found in microstructure of samples OQ from above 1133 K. This was in agreement with the results of dilatometry which showed complete γ region above 1123 K. Very small amount of α_{ac} was observed in the 1203 K OQ samples. It was observed in Fig. 3c that the sample austenitized at 1273 K completely transformed into needle-shaped α_M upon oil quenching. Plate shape morphology was now partially replaced by lath (needle-shaped) morphology due to higher austenitizing temperature. Moreover, numbers of α_M packets were decreased with increasing γ grain size (Fig. 3d). ASTM grain size no. of 1273 K OQ sample was found to be 9 (22 μm grain dia.). Retained γ was not visible in 1273 K and 1323 K OQ samples (Fig. 3c, d). The decreasing amount of retained γ above 1273 K was associated with γ grain growth. Increase in prior γ grain size (PAGB) resulted in increased hardenability. However, it was interesting to observe that some percentage of block-type granular bainite (α_{Gb}) was present within α_M matrix (Fig. 3c). Granular bainite α_{Gb} was formed during slack quenching (i.e. quenching at a rate slower than the critical cooling rate) [23]. This type of bainite usually formed inadvertently during Q&T treatment due to insufficient alloy content, thicker sizes or slow quench speed. However, the predominant structure was α_M for all quenching conditions. It was also observed that the grain size was increased from 15 μm at 1203 K to 30–35 μm at 1323 K (Fig. 3d). It was seen in Fig. 3d that the higher austenitizing temperature resulted only in the grain growth. As it was very difficult to distinguish between α_{Gb} and α_M by conventional etching techniques, therefore heat-tinting technique was employed to reveal α_{Gb} in α_M matrix. Figure 5a and b showed the optical micrographs of as-quenched samples heat tinted to reveal α_{Gb}. Bainite appeared darker than α_M and retained γ appeared white with this technique (Fig. 5a, b).

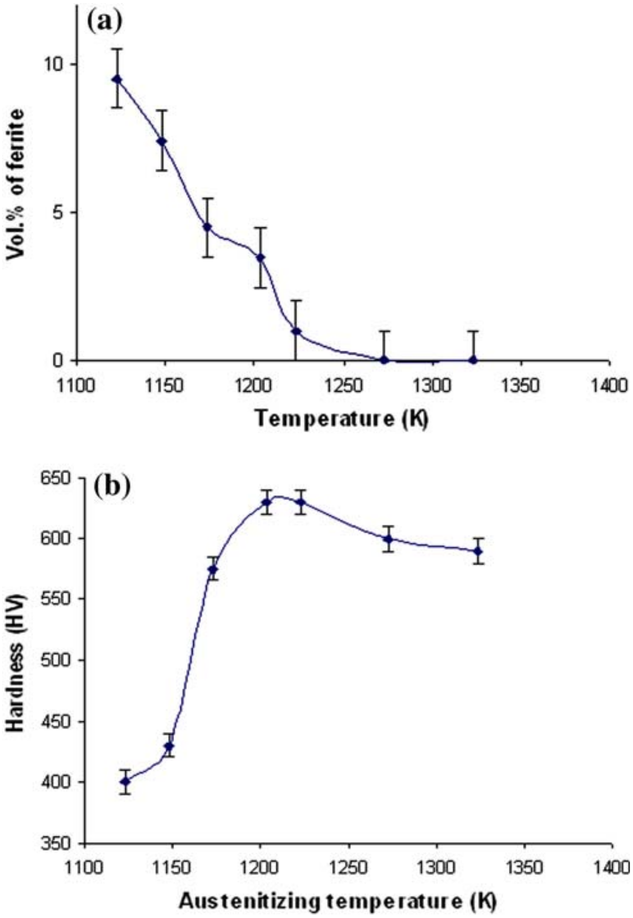

Fig. 5 Heat-tinted optical micrographs showing mixed microstructure produced in OQ samples (α_M martensite, α_{Gb} granular bainite, γ retained austenite)

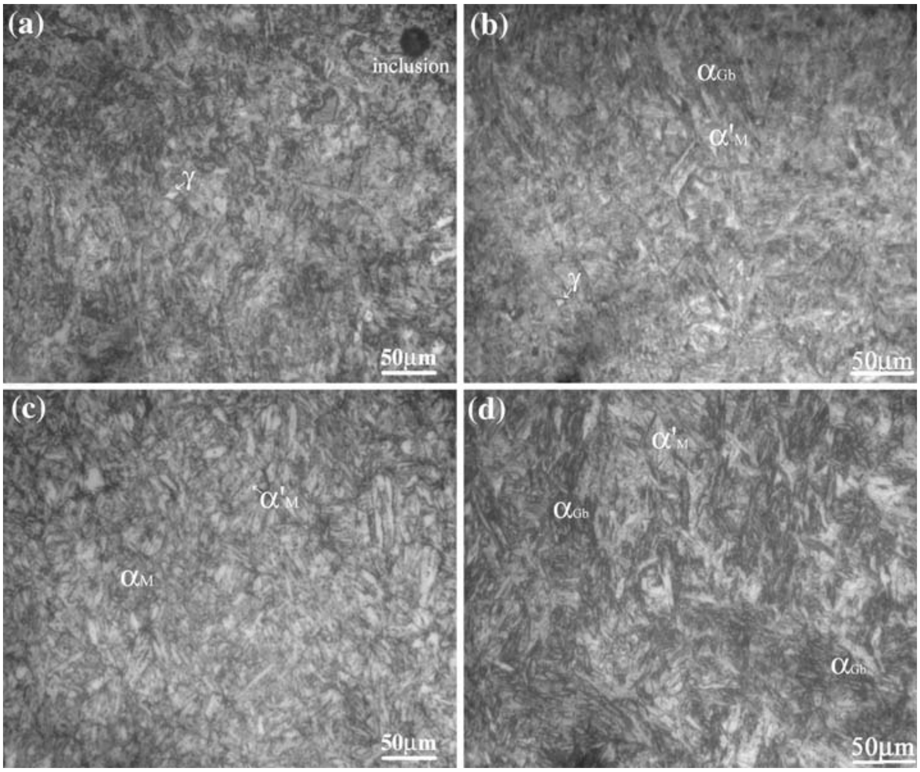

Fig. 6 Optical micrographs of samples. **a** Q&T at 1203/473 K for 2 h, **b** Q&T at 1203/573 K for 3 h, **c** Q&T at 1203/773 K for 3 h, and **d** Q&T at 1273/573 K for 3 h ($\alpha'M$ tempered martensite, α_{Gb} granular bainite, α_b bainitic ferrite, γ retained austenite)

Figure 6 showed the range of optical micrographs taken after various tempering treatments. It was observed that the tempering in the range of 473–573 K for any time period after oil quenching from either 1203 K or 1273 K did not affect the microstructure (Fig. 6a, b, d). Low temperature tempering resulted in the relief of residual stresses induced during quenching, reduction in dislocation density, and precipitation of excess entrapped C in the form of transition carbide (also called ε carbide, i.e., $Fe_{2.4}C$). However, ε carbide particles were so small that they were not resolved by OM. Supersaturated α_M was transformed to low-C α_M and the structure looks less darker than as-quenched structure (Fig. 6b). Auto-tempered martensite was also found in tempered samples as shown in Fig. 6b, c. As the Ms temperature of the steel was sufficiently high therefore extensive redistribution of carbon atoms was occurred after transformation while the steel was still cooling and resulted in tempering of already formed α_M. Figure 6c showed mixed microstructure containing α_{Gb}, α_M, and α'M in 1203 K OQ sample tempered at 773 K for 3 h. No major change in microstructure was observed even after raising the tempering temperature to 773 K except that the structure appeared light etched (Fig. 6c). Packet structure of α_M consisting of narrow almost parallel plates was also revealed in samples tempered at 773 K (Fig. 6c). Figure 6d showed the mixed microstructures produced in 1273 K OQ sample tempered at 573 K for 3 h. It was also noticed that the amount of α_{Gb} was relatively higher in 1273 K OQ samples than 1203 K OQ samples, because of absence of retained γ in 1273 K OQ samples (Fig. 6d). Higher austenitizing temperature caused γ grain growth and more homogeneous structural composition which when quenched transformed into α_{Gb} and α_M mixed microstructure with very negligible amount of retained γ; the fact also confirmed from XRD results. Moreover, high austenitizing temperature replaced the plate-type α_M by lath-type α_M (Fig. 6d).

Generally the precipitation of Fe_3C starts at 473 K with subsequent dissolution of transition carbide [24, 25]. Fe_3C decorates the grain boundaries or interlath boundaries of α_M. But in present case, Fe_3C was not observed in optical micrographs even after tempering up to 773 K. The reason for absence of Fe_3C precipitation was high Si in steel, which delayed the formation and coarsening of Fe_3C during high temperature tempering because of its low solubility in γ. The effect of Si on precipitation of cementite from α_M and α_b and on bainitic transformations is well known [24–32].

Finer details of the microstructure were examined by SEM and presented in Fig. 7. Figure 7a revealed the composite microstructure formed in 1203 K OQ sample. Granular bainite was based on the matrix of polygonal α and the granules distributed within it were composed of α_M and γ. The presence of significant amount of α_{Gb} was attributed to high Si of the steel, which lowers the Bs temperature, decreases the free energy of α, and thus increases the driving force for bainite reaction [31, 32]. Furthermore, Cr and Mn are also known to promote bainite formation in steel during

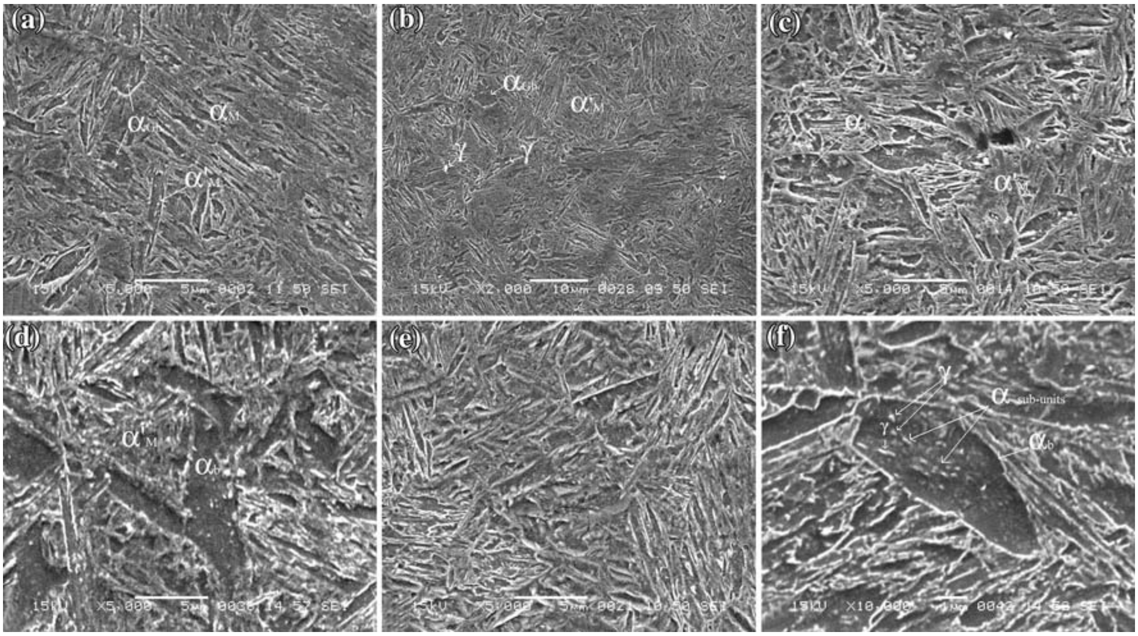

Fig. 7 SE micrographs showing mixed microstructure in samples **a** OQ from 1203 K, **b** Q&T at 1203/523 K for 2 h, **c** Q&T at 1203/573 K for 3 h, **d** Q&T at 1203/773 K for 3 h, **e** Q&T at 1273/673 K for 2 h, and **f** Q&T at 1273/773 K for 2 h ($\alpha'M$ tempered martensite, $\alpha\alpha_b$ bainitic ferrite, α_{Gb} granular bainite, γ retained austenite)

continuous cooling [33]. Bainite can also be produced as result of decomposition of retained γ during tempering, but from XRD results retained γ was found thermally stable up to 673 K. Therefore, observed α_{Gb} was actually formed during slack quenching rather than from decomposition of γ. The α_{M} packet size was measured to be 7–11 μm in length and about 6–9 μm wide. However, the packet size was not same in whole structure cause of compositional heterogeneity and formation of other microconstituents. Martensite packets were separated by low angle grain boundaries. Each packet contained several laths oriented in similar direction. Martensite packet size was related to austenitizing temperature and found increasing with an increase in temperature. As the austenitizing temperature was increased, the γ grain size also increased and structure became more homogenous. Upon quenching, this large grained γ transformed to α_{M} having relatively large packets and laths. Interesting feature observed in SEM micrographs of tempered samples was the presence of carbide-free α_{b} (CFB), clearly shown in Fig. 7c,d. The CFB was distinguished from α_{Gb} because of its widmanstatten morphology. CFB was nucleated from PAGB in the form of sheaf such that each sheaf oriented in different direction to accommodate transformation strains (Fig. 7c,d) [24]. Each sheaf of α_{b} contained several sub-units of carbide-free α separated by thin films of C-enriched residual γ (Fig. 7f). Presence of CFB was related to Si which is relatively insoluble in Fe_3C and therefore retards the conversion of Fe_3C from ε carbide during tempering [34, 35]. Bainitic ferrite formed during quenching rejects C (by diffusion) into the surrounding γ thereby reducing its Ms temperature and promoting its stability. Length of the CFB sheaves was 6–11 μm and width was ranging from 800 nm to 2 μm. Length of both α_{M} packets and CFB sheaves was limited by PAGB [24]. Figure 7e showed the micrograph of 1273 K OQ sample followed by tempering at 673 K for 2 h, no sign of Fe_3C precipitation was observed. The reason for absence of Fe_3C particles was already discussed in preceding paragraphs. In contrast, in medium C steels containing only nominal amount of Si (about 0.3%) the interlath film of γ decomposes to continuous interlath carbides during tempering in the range of 473–623 K.

X-ray diffraction

XRD results of selected samples were given in Fig. 8a–d, showing α_{M} and γ peaks arising from different hkl planes and having varying intensities. XRD curve of 1203 K OQ sample was shown in Fig. 9a. Austenite peaks were coming from (111)γ, (200)γ, and (220)γ but the peaks were difficult to recognize due to their low intensity and high background noise. The maximum vol% of γ was measured to be 24%, whereas average C content of retained γ was calculated about 1.5%. High Si and Mn content of the steel and bainitic transformation encouraged the retention of large vol% of γ on quenching. On the other hand, no retained γ was detected in 1273 K OQ samples as shown in Fig. 8b. This was in conformance with the results of microscopy. Figure 8c, d showed the diffraction pattern of 1273 K OQ samples tempered at 573 and 773 K for 2 h, respectively. Retained γ was found to be thermally stable during tempering up to

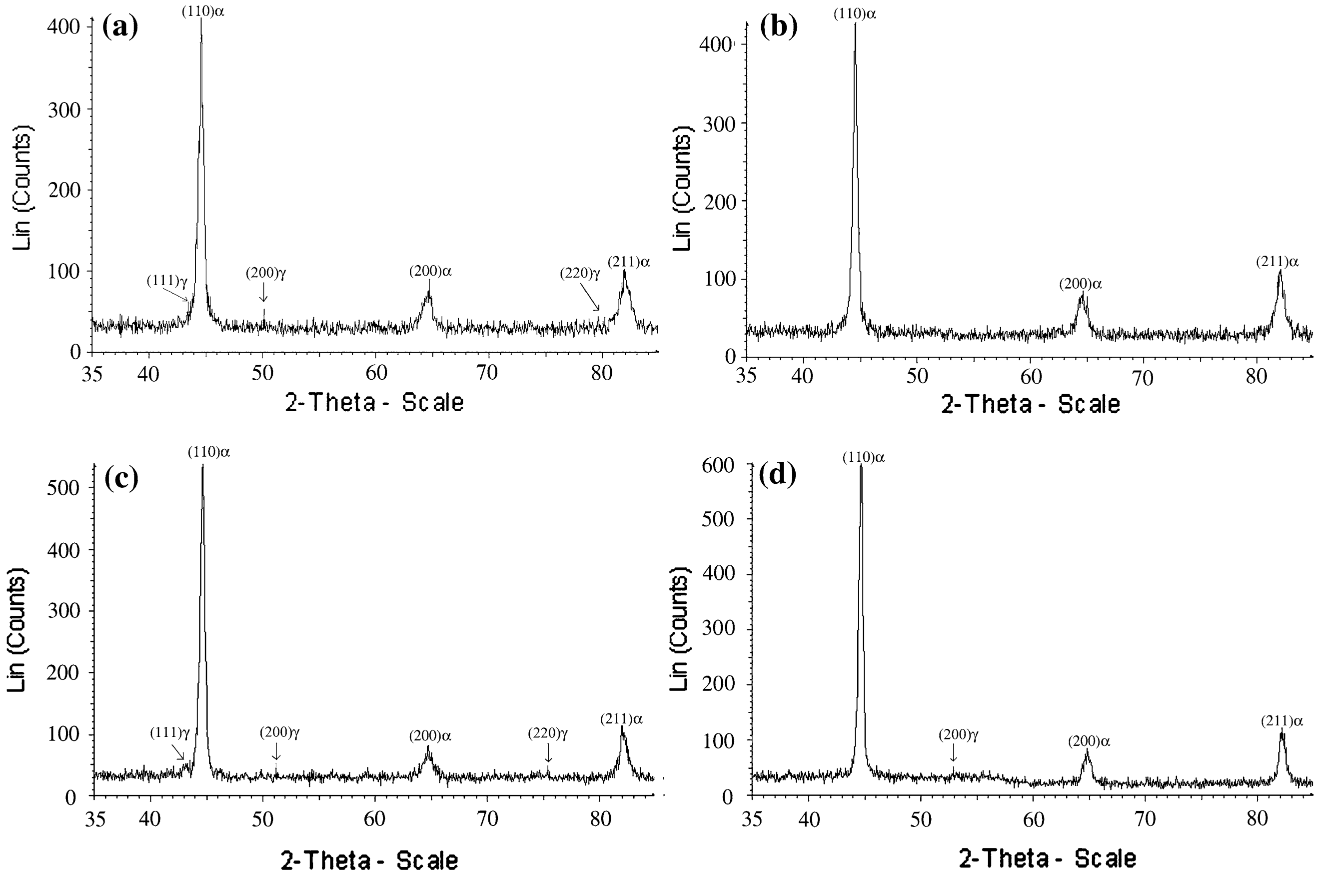

Fig. 8 XRD curves of samples **a** OQ from 1203 K, **b** OQ from 1273 K, **c** Q&T at 1203/573 K for 2 h, and **d** Q&T at 1203/773 K for 2 h

723 K. Furthermore, tempering time had no affect on retained γ stability and percentage. The vol% of γ was reduced to 16% for sample tempered at 773 K for 2 h. The (220)γ peak was also absent in the sample tempered at 773 K for 2 h (Fig. 8d). Moreover, the C content of the retained γ was also found slightly decreased at 773 K. Similar behavior is reported by many researchers while working on C–Si–Mn steels [36–38]. The lesser amount of γ pointed out that some percentage of the γ was probably decomposed into α and carbide at higher tempering temperature, but carbide was not observed in microscopy. The stability and retention of large vol% of γ during tempering was attributed to the C-enrichment of γ and high Si content of the steel (as Si retards the carbide precipitation due to its low solubility in γ). From XRD results, it was assumed that most of the retained γ exists in C-enriched α_b; since very little vol% of block-type γ was revealed by microscopy.

Mechanical properties

The response of Q&T treatments on room temperature hardness, yield strength (YS), ultimate tensile strength (UTS), ductility (in terms of %elongation and %reduction), and charpy V-notch (CVN) impact energy with varying tempering temperatures and time periods were plotted in Fig. 9a–f. Error in readings of hardness was about ±5 HV, YS, and UTS about ±25 MPa, %E and %R about ±1% ,and CVN impact energy about ±1 J. Figure 9a–c exhibited the decrease in hardness, YS, and UTS with increasing tempering temperature and time for both 1203 K and 1273 K OQ samples. However, it was observed that the hardness slightly increased for the 1203 K and 1273 K OQ samples tempered at 573 K for any time period (Fig. 9a). Similarly, it was seen in Fig. 9b, c that the YS and UTS curves were raised for both 1203 K and 1273 K OQ samples tempered at either 523 K for 3 h or 573 K for 2 h. Maximum average hardness about 600 HV, YS about 1760 MPa, and UTS about 1890 MPa was achieved for 1203 K OQ samples tempered in between 473 and 573 K for 2–3 h. Whereas, hardness, YS, and UTS were decreased down to 450–470 HV, 1250–1450 MPa, and 1400–1500 MPa, respectively, for the samples tempered at 773 K for 2–3 h for all OQ conditions. Temperature and time are independent variables in tempering of steels, and that one can obtain the same results either by decreasing temperature and increasing time or by raising temperature and decreasing time. Same

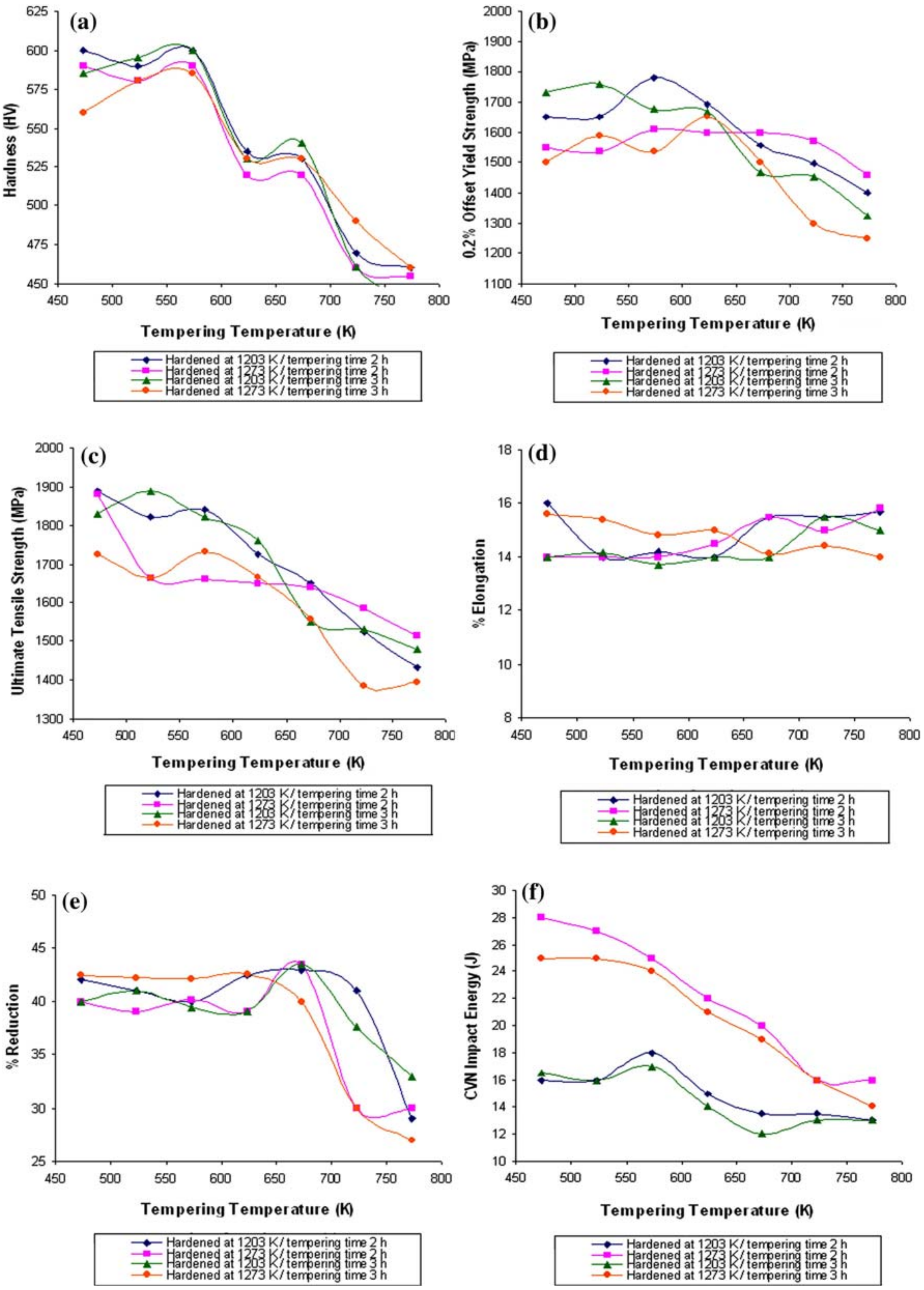

Fig. 9 Graphs showing variation in mechanical properties in response to tempering temperature and time **a** hardness, **b** 0.2% offset YS, **c** UTS, **d** %E, **e** %R, and **f** impact absorbed energy

phenomenon was observed in this work; increase in tempering time at any temperature resulted in decrease in hardness and strength. Decrease in hardness and strength with increasing tempering temperature or time was related to the recovery-induced reduction in dislocation density and coarsening of transition carbides. The slight increase in hardness and strength in range of 523–573 K were attributed to the precipitation of transition carbides. Transition carbides are coherent with the matrix therefore hinders the motion of dislocations and thus raises the hardness and strength of the steel. Moreover, Si is also known to have a much greater effect in range of 473–593 K than at other tempering temperatures because it retards the softening by inhibiting dissolution or conversion of transition carbides to cementite during this range [39, 40]. Beneficial effect of Si on tempering resistance at low tempering temperatures was confirmed from these results. The hardness and strength of 1203 K OQ and tempered samples were slightly greater than 1273 K OQ and tempered samples because of the presence of fine α_M and CFB composite microstructure. Lower hardness and strength values of 1273 K OQ samples was attributed to the larger α_M packet size plus higher amount of α_{Gb} (Fig. 9a–c). Strength of α_{Gb} is lower than CFB. However, change in hardness and strength properties was more uniform in 1273 K OQ and tempered samples because of more homogenous microstructure obtained by high temperature austenitizing. The YS/UTS ratio was measured to be 0.86–0.92 for 1203 K OQ samples tempered at 473–532 K and 0.96–0.98 for samples tempered at 573–773 K for 2–3 h. Similarly, YS/UTS ratio was 0.83–0.92 for 1273 K OQ samples tempered at 473–523 K and 0.96–0.98 for 573–773 K tempered samples. Figure 9d–f showed the results of %E, %R, and CVN impact energy with respect to tempering temperatures. Maximum elongation about 16% was achieved in 1203 K and 1273 K OQ samples tempered at 473 K for 2 h. No appreciable change in %E was observed for all Q&T conditions; %E curve was almost stable despite of increasing tempering temperature (Fig. 9d). Similar trend was observed for %R up to 623 K for all Q&T conditions. However, sharp decline in %R curve was observed with increasing tempering temperature above 623 K (Fig. 9e). It was noted that the %R was reduced about 25–30% when samples were tempered in range of 623–773 K for any time period. This significant decrease in %R was the consequence of TME. Maximum %R of 43% was achieved in 1273 K OQ samples tempered at 473 K for 3 h (Fig. 9e). It was also noted that the 1273 K OQ samples were more ductile in terms of %E and %R than 1203 K OQ samples regardless of the tempering treatments. From the results of CVN impact test seen in Fig. 9f, it was deduced that the impact energy of 1203 K OQ samples initially raised with increasing tempering temperature up to 573 K and then decreased on high tempering temperatures irrespective of tempering time. Peak impact energy of 18 J was obtained for the 1203 K OQ samples tempered at 573 K for 2 h. Impact energies reduced to 13 J when the 1203 K OQ samples were tempered at 773 K for 2–3 h. On the other hand, the impact energy of 1273 K OQ and tempered samples decreased with increasing temperature. However, sudden fall in impact energy curve was observed for samples tempered at 623 K or above for any time period (just like in 1203 K OQ samples). In all cases, 1273 K OQ samples showed much higher impact energies than 1203 K OQ samples, but reduction in impact energy of 1273 K OQ samples was more drastic (Fig. 9f). Maximum impact energy of 28 J was achieved for 1273 K OQ samples tempered at 473 K for 2 h which decreased down to 15 J on high tempering temperature, i.e., 773 K. Greater decrease in impact energy of 1273 K OQ and tempered samples was attributed to their coarser grain size. Coarse grain size is known to embrittle more than fine grain [41]. The significant reduction in impact energies of samples when tempered in between 623 and 773 K was attributed to TME. TME refers to the phenomenon in which the impact energy of the Q&T steel sharply reduced when tempered in between 473 and 623 K due to precipitation of brittle Fe_3C phase between laths of α_M and the segregation of harmful solute elements (like S, P, Sb, etc.) on PAGB [42, 43]. The interlath Fe_3C arrays acts as stress raisers and promotes crack propagation through them. Alloy steels are most susceptible to TME and the co-segregation of the alloying elements with the impurities to PAGBs has been documented [44]. Among alloying elements, Mn and Cr are known to enhance the detrimental effect of P which is a major embrittling element in steel [45, 46]. TME can also cause by deformation-induced transformation of retained γ into brittle α_M [47]. However, XRD results have showed that the retained γ was thermally stable up to 723 K. Hence, Si in the steel delayed the TME onset temperature above 623 K [48] by inhibiting interlath Fe_3C precipitation, but severe loss in impact toughness was occurred above 623 K that was associated with the combined effect of P segregation on the PAGBs and the formation of interlath Fe_3C. But interlath Fe_3C was probably so fine that it was not resolved by SE microscopy.

Fractography

Fractography of all CVN impact specimens was carried out to reveal the nature and morphology of fracture; however, results of only selected representative specimens were included here. Outer edges of all fractured specimens showed shear angular surface as seen in Fig. 10a. The central portion of the specimens exhibited different types of fractures. Figure 10a showed the stereo fractograph of central portion of specimen tempered at 473 K for 2 h, fractured in ductile manner with impact absorbed energy

Fig. 10 Stereomicroscope fractographs of CVN impact specimens OQ and tempered at **a** 473 K for 2 h, **b** 573 K for 3 h, and **c** 773 K for 3 h (Magnification: ×25)

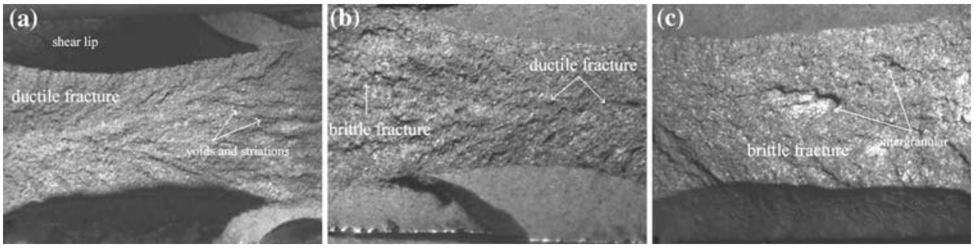

about 25 J. Fracture was appeared dull with too many voids and striations, reflecting typical ductile fracture mode. Striations were indicating the direction of crack propagation. Figure 10b represents the mixed mode of fracture (i.e. partially ductile dimple and partially brittle cleavage) occurred in samples tempered at 573 K for 3 h. Shinny facets of the fracture indicate the brittle mode while the ductile area was dull and contains voids and cavities (Fig. 10b). Specimens tempered above 623 K exhibited brittle fracture (shinny facets) with sharp drop in impact energy, i.e., <15 J (Fig. 10c). This type of fracture occurred because of TME as already seen from the impact test results (Fig. 9f). From the optical fractography, it was observed that the both 1203 K and 1273 K OQ specimens fractured in similar manner after tempering. Furthermore, tempering time employed in this work had no significant affect on fracture appearance.

Figure 11a–f corresponds to the high magnification SEM fractographs of central region of impact specimens. Figure 11a, b showed the ductile transgranular fracture containing many coarse dimples with bright white surroundings and few small voids on the entire fractured surface. These dimples and voids were expected to nucleate at NMIs or possibly on retained γ. The dimples were ranging in size from 17 to 21 μm for 1203 K OQ specimens and 40–52 μm for 1273 K OQ specimens. Presence of comparatively coarse dimples in 1273 K OQ specimens indicated that more plastic deformation occurred prior to fracture. 1203 K OQ specimens tempered in between 573 and 623 K exhibited mixed transgranular fracture with primarily quasi-cleavage fracture areas and some ductile shallow dimple surfaces, as shown in Fig. 11c. The shallow dimples indicated that relatively less energy was absorbed by the specimen during plastic deformation prior to fracture. Brittle intergranular fracture with some quasi-cleavage areas was observed for specimens tempered above 623 K regardless of the austenitizing temperature before quenching, as shown in Fig. 11d, e. The dominant fracture mode was intergranular when the specimens tempered above 623 K for any time period (Fig. 11e). These observations confirmed the TME of steel. Ductile-to-brittle fracture transition temperature was shifted to higher temperature due to TME and fracture mode

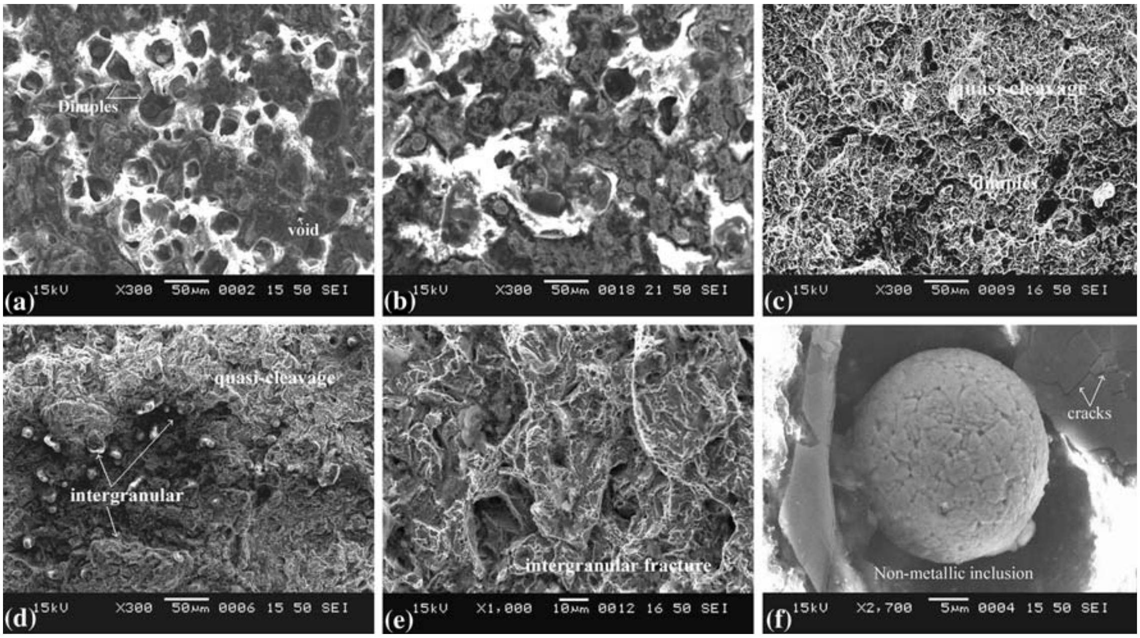

Fig. 11 SEM fractographs of CVN impact specimens. **a** Q&T at 1203/473 K for 2 h, **b** Q&T at 1273/473 K for 2 h, **c** Q&T at 1203/623 K for 2 h, **d** Q&T at 1273/773 K for 2 h, **e** brittle intergranular fracture as a result of TE, and **f** NMI responsible for crack initiation and fracture

was changed from transgranular to intergranular. In 1273 K OQ and tempered specimens intergranular microcracks were large (due to large γ grain size) and crack coalescences rather easily. Embrittling effect of impurities was enhanced by increasing the PAGB. The possibility of intergranular fracture therefore increases with increasing austenitizing temperature. No sign of intergranular fracture was observed in specimens tempered at <623 K. This is in agreement with the fact that there was no loss in impact energy of samples tempered below 623 K. An interesting feature fortunately observed in few specimens fractured in ductile transgranular manner was the presence of NMI inside the dimple (Fig. 11f). Brittle inclusion acted as crack initiation sites along a brittle interface, as evident in Fig. 11f. The voids were formed at these inclusions and then grew into dimples which ultimately fractured. Microvoids were also expected to be formed at brittle carbide particles precipitated either during quenching or tempering. Figure 11f clearly showed the micro-cracks nucleating adjacent to the brittle NMI. The thought of initiating of cracks and voids from the NMI was thus confirmed from the SEM fractographs. Hence, the inadequate cleanliness of the steel resulted in formation of brittle inclusions which in combination with TME adversely affected the toughness-related properties. It is therefore highly recommended that the inclusion content of ultrahigh strength steels for critical applications should be kept as low as possible by modifying steel making practice (e.g. use electro-slag remelting (ESR).

Figure 12 showed the elemental mapping results of the specimen fractured in intergranular manner. The distribution and segregation of selected elements on intergranular and transgranular cleavage facets was clearly seen in Fig. 12. Elemental map of only C, P, Cr, and Mn were presented here. White spots represented the elements, whereas the brightness of spots reflected the concentration of particular element in that region. Black areas indicated the depletion of element in that region. Co-segregation of C and P was observed, whereas Cr and Mn were found uniformly distributed throughout the fracture. Carbon was found to be segregated on both intergranular and transgranular cleavage facets. High concentration of P on intergranular facet confirmed that the TME was resulted because of P segregation to PAGB. As the steel under investigation contained about 0.02%P, therefore P segregation was obvious. P atoms migrated to PAGB due to differences between strain energies of grains and grain boundaries. Intergranular segregation decreased the intergranular cohesive strength of grain boundaries and weakened them. Grain boundaries were therefore no longer strong to act as barrier to crack propagation and hence intergranular decohesion occurred. Hence, %P should be kept as minimum as possible in Q&T steels to prevent intergranular fracture.

Conclusions

Effect of Q&T treatments on development of microstructure and mechanical properties of ultrahigh strength 0.3%C Si–Mn–Cr–Mo low alloy steel was studied. Main conclusions drawn were as follows:

1. Microscopy and SEM–EDS results revealed NMIs of Type A (sulfide) and Type C (oxide and silicates) randomly distributed throughout the steel. This reflected the inadequate cleanliness of the alloy.
2. Mixed microstructures ($\alpha_{ac} + \alpha_M + \alpha_b +$ retained γ) were produced upon quenching from 1203 K and 1273 K. The vol% of these phases varies with austenitizing temperature and cooling rate.
3. From the results of XRD, max% of retained γ was found to be 24% for 1203 K OQ samples.

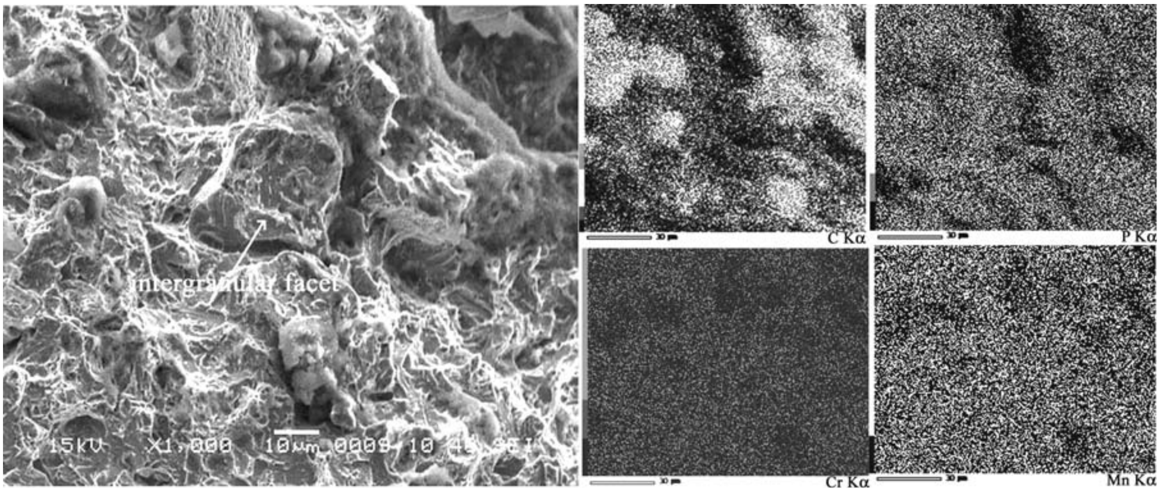

Fig. 12 SEM fractograph showing intergranular fracture (as a result of TME) along with elemental mapping

4. Tempering in between 473 and 623 K for 2–3 h did not significantly change the microstructure for both 1203 K and 1273 K OQ samples except stress relieving and reduction in dislocation density. However, recovery of dislocations and change in morphology of α_M and α_b phases was observed for samples tempered at 773 K for 2 and 3 h. Moreover, retained γ was found stable up to 723 K from results of microscopy and XRD.
5. SEM examination revealed the presences of α'M, α_{Gb}, CFB, and C-enriched γ in the Q&T microstructures. CFB was attributed to high Si content of the steel.
6. Optimum combination of mechanical properties were achieved for 1203 K OQ samples tempered in between 473 and 573 K for 2–3 h. Peak hardness of about 600 HV, 0.2% offset YS about 1760 MPa and UTS about 1890 MPa was achieved with %E and %R about 15 and 42%, respectively.
7. CVN impact energies of 1273 K OQ samples were found higher than 1203 K OQ samples for all tempering temperatures and time. Maximum impact energy of 28 J was achieved for 1273 K OQ sample tempered at 473 K.
8. Hardness, YS, and UTS were found decreasing with increasing tempering temperature. In contrast, %E, %R, and impact energy were found almost stable up to 573 K and then decreases. Significant reduction in CVN impact energies were observed for samples tempered above 623 K, attributed to TME.
9. SEM fractographs of impact specimens showed primarily ductile-dimple fracture for samples tempered below 623 K, brittle quasi-cleavage fracture for samples tempered between 623 and 723 K and brittle intergranular fracture for samples tempered above 723 K. Elemental mapping showed the segregation of P on PAGBs. Cracks were mostly found to be nucleated from NMIs, hence inclusions were found detrimental to impact toughness.

Acknowledgements The authors wish to thank Mr. Muhammad Saraf (Deputy Chief Manager) and Dr. Sajid Mirza (Senior Chief Manager) for their valuable suggestions and guidance and Mr. Raza Hussain (Chairman SUPARCO) for their approval and provision of facilities. Authors also like to acknowledge the technical assistance and meaningful discussions made by Mr. Badar-ul-Hassan (Technical Officer) throughout the experimental work.

References

1. Sreekumar K, Murty MSP, Natarajan A, Sinha PP (1982) Trans Indian Inst Met 35:349
2. Tartaglia JM (2009) J Mater Eng Perform (published online)
3. Tomita Y, Okabayashi K (1983) Met Trans A 14A:485
4. Thomas TS, Hickey CF (1989) J Heat Treat 7(1):49
5. Holt JM, Mindlin H, Ho CY (1996) Structural alloys handbook. CINDAS/Purdue University, USA
6. Youngblood JL, Raghavan M (1977) Metall Trans A 8A:1439
7. Khan SA, Bhadeshia HKDH (1990) Mater Sci Eng A 129:257
8. Rajan KM, Narasimhan K (2002) J Mater Eng Perform 11:444
9. R. Steiner (1993) ASM handbook, 10th edn, vol 1. ASM International Metals Park, OH
10. Steven W, Haynes AG (1956) J Iron Steel Inst 183:349
11. Krauss G (1990) Principles of heat treatment and processing of steels. ASM Int, USA, pp 43–87
12. Roberts VJ (1997) Metall Trans 1:3287
13. Ohtani H, Terasaki F, Kunitake T (1972) Trans Iron Steel Inst Jpn 12:118
14. Maropoulos S, Paul JDH, Ridley N (1993) Mater Sci Technol 9:1014
15. Cullity BD, Stock SR (2001) Elements of X-ray diffraction. Prentice Hall, USA
16. Ridley N, Stuart H, Zwell L (1961) Trans AIME 245:1834
17. Vorob'eva EP, Chadov GA, Kansafarova TT, Gervas'ev MA (2000) Met Sci Heat Treat 42(11–12):444
18. Kiessling R, Lange N (1976) Non-metallic inclusions in steel. The Metal Society, London, pp 50–110
19. Jie S, Tian-dong X, Xiao-jun W, Xiao-chun F (2007) Trans Nonferrous Met Soc China 17:1165
20. Bohmer HJ (1993) ASTM STP 1195. American Society for Testing and Materials, Philadelphia, pp 211–221
21. Gigovic-Gekic A, Oruc M, Vitez I, Vujicic B (2009) Metallurgija 48(1):29
22. Li-feng Zhang (2004) Shandong Metall 26(6):1 (in Chinese)
23. Kremnev LS, Svishchenko VV, Cheprasov DP (1997) Met Sci Heat Treat 39(9–10):367
24. Bhadeshia HKDH (2002) Bainite in steels, 2nd edn. Institute of Materials, London
25. Peet M, Babu SS, Miller MK, Bhadeshia HKDH (2004) Scripta Mater 50:1277
26. Kozeschnik E, Bhadeshia HKDH (2008) Mater Sci Technol 24(3):343
27. Pickering FB (1979) Phase transformations. Institution of Metallurgists, London, 2 VI 7
28. Deliry J (1965) Mem Sci Rev Metall 62:527
29. Pomey J (1966) Mem Sci Rev Metall 63:507
30. Bhadeshia HKDH, Edmonds DV (1979) Metall Trans A 10A:895
31. Sandvik BPJ (1982) Metall Trans A 13A:777
32. Bhadeshia HKDH (1982) J Phys Colloque 43:443
33. Wang J, Vander Wolk PJ, Vander Zwaag S (2000) J Mater Sci 35:4393. doi:10.1023/A:1004865209116
34. Nam WJ, Kim DS, Ahn ST (2003) J Mater Sci 38:3611. doi:10.1023/A:1025625330442
35. Zhang M, Qian J, Haicheng G (2007) J Mater Eng Perform 16(5):635
36. Tomita Y (1995) J Mater Sci 30:105. doi:10.1007/BF00352138
37. Jacques PJ (2004) Curr Opin Solid State Mater Sci 8:259
38. DeCooman BC (2004) Curr Opin Solid State Mater Sci 8:285
39. Allten G, Payson P (1953) Trans Am Soc Met 45:498
40. Shih H, Averbach BL, Cohen M (1956) Trans Am Soc Met 48:66
41. Capus JM (1962) J Iron Steel Inst 200:922
42. Kula EB, Anctil AA (1969) J Mater 4:817
43. Briant CL (1989) Mater Sci Technol 5:138
44. Vander Voort GF (1993) ASM handbook, vol 1, 10th edn. ASM Int, Metals Park, OH
45. Schulz BJ Jr, McMahon CJ (1972) ASTM STP 499. American Society for Testing and Materials, Philadelphia, pp 104–135
46. Low JR (1968) Trans AIME 242:14
47. Horn RM, Ritchie RO (1978) Metall Trans A 9A:1039
48. Bhadeshia HKDH, Edmonds DV (1979) Met Sci 13:325